Benafan, O.; Garg, A.; Noebe, R.D.; Bigelow, G.S.; Padula, S.A.;
Gaydosh, D.J.; Schell, N.; Mabe, J.H.; Vaidyanathan, R.:

Mechanical and functional behavior of a Ni-rich Ni50.3Ti29.7Hf20 high temperature shape memory alloy

In: Intermetallics (2014) Elsevier

DOI: 10.1016/j.intermet.2014.02.006

Mechanical and functional behavior of a Ni-rich $Ni_{50.3}Ti_{29.7}Hf_{20}$ high temperature shape memory alloy (*to be submitted to: Intermetallics*)

O. Benafan[a,*], A. Garg[b,a], R.D. Noebe[a], G.S. Bigelow[a], S.A. Padula II[a], D.J. Gaydosh[c,a], N. Schell[d], J.H. Mabe[e], R. Vaidyanathan[f]

[a]NASA Glenn Research Center, Structures and Materials Division, Cleveland, OH 44135, USA
[b]University of Toledo, Toledo, OH 43606, USA
[c]Ohio Aerospace Institute, Cleveland, OH 44142, USA
[d]Institute of Materials Research, Helmholtz-Zentrum Geesthacht, Max-Planck-Str. 1, D-21502 Geesthacht, Germany
[e]The Boeing Company, Seattle, WA 98124, USA
[f]Advanced Materials Processing and Analysis Center, Materials Science and Engineering Department, University of Central Florida, Orlando, FL 32816, USA

Abstract – The mechanical and functional behavior of a Ni-rich $Ni_{50.3}Ti_{29.7}Hf_{20}$ high temperature shape memory alloy were investigated through combined *ex situ* macroscopic experiments and *in situ* synchrotron x-ray diffraction. Isothermal tension and compression tests were conducted at various temperatures, while isobaric thermomechanical cycling experiments were conducted at various stresses. Isothermal testing of the martensite phase revealed no plastic strain up to the test limit of 1 GPa and a near-perfect superelastic behavior up to 3% applied strain above the austenite finish temperature. Excellent dimensional stability with greater than 2.5% actuation strain and no accumulation of residual strains (at stress less than -500 MPa) were observed during isobaric thermal cycling experiments. The absence of residual strain development during thermomechanical cycling was confirmed by the lattice strains, calculated from the x-ray spectra. Even in the untrained condition, the material exhibited little or no history or path dependence in behavior, consistent with measurements of the bulk texture through synchrotron x-ray diffraction. Post deformation cycling revealed the limited conditions under which a slight two-way shape memory effect (TWSME) was obtained, with a maximum of 0.6% two-way shape memory strain after thermomechanical cycling under -700 MPa.

Keywords: High temperature shape memory alloy, NiTiHf, synchrotron x-ray diffraction, actuation strain, TWSME, precipitation hardening, superelasticity, shape memory behavior.

Highlights (mandatory for this Journal):

- NiTiHf HTSMA is resistant to plastic deformation at stress greater than 1 GPa.
- NiTiHf HTSMA exhibits completely stable shape memory behavior under 500 MPa stress.
- Thermomechanical stability confirmed through in situ synchrotron x-ray diffraction.
- 0.6% two-way shape memory strain developed through -700MPa thermomechanical training.

*Corresponding author: Tel.: +1 (216) 433 8538; fax: +1 (216) 977-7132.
E-mail address: othmane.benafan@nasa.gov (O. Benafan).

1. Introduction

High temperature shape memory alloys (HTSMAs) have vast potential in a wide range of applications spanning from aerospace to automotive to energy exploration industries, amongst others. The majority of these applications demand large actuation capability, higher transformation temperatures (above 100 °C) and stable response, which restricts the existing possibilities to a small group of alloys. Of these alloys, NiTi-based HTSMAs such as NiTiPd [1], NiTiPt [2-4], NiTiZr [5, 6] and NiTiHf [6-10] have shown significant scientific and technological merit in the last few years. A comprehensive review of select HTSMAs can be found in Ref. [11]. In particular, NiTiHf has been developed as a low cost alternative when compared to NiTi-X (X = Pt, Pd, Au), and just recently, Ni-rich NiTiHf alloys were found to exhibit superior properties and dimensional stability through compositional and aging control [7-10, 12, 13]. This was accomplished by developing a slightly Ni-rich composition with 20 at.% Hf, that is capable of being precipitation strengthened when subjected to an ageing heat treatment to produce fine, nanometer size precipitates. The precipitates strengthen the alloy providing high resistance to dislocation motion while allowing a nearly unobstructed phase transformation. Thus, it is necessary to characterize both the macroscopic and microstructural behavior of the Ni-rich NiTiHf to optimize the alloy and its processing and to develop an appropriate database to transition this material into engineering components.

Previously, the shape memory and superelastic behaviors of Ni-Rich $Ni_{50.3}Ti_{29.7}Hf_{20}$ (at.%) alloy were determined under tension and compression for a limited number of thermomechanical/mechanical cycles [10]. Similarly, compressive testing was performed on the same alloy at temperatures above the austenite finish (A_f) temperature to study the effect of aging on the stress-induced transformation and plasticity, but also only for a few cycles [8]. In single

crystal form, the effects of applied stress and testing temperatures were evaluated along the [111] orientation with stress levels up to 1000 MPa [9]. From a microscopic perspective, *in situ* neutron diffraction was used to investigate the role of the fine precipitates in developing texture, internal strains, and other microstructural features during tensile and isobaric thermomechanical testing [7]. In all cases [7-10], the alloy exhibited outstanding strength and stability (lack of residual strain) during transformation under isothermal and isobaric conditions. The structure of the precipitate phase, responsible for these benefits, has recently been identified by Yang et al. [12] using conventional electron diffraction, high-resolution scanning transmission electron microscopy (STEM) and three-dimensional atom probe tomography to be a face-centered orthorhombic lattice with a = 1.264 nm, b = 0.882 nm, c = 2.608 nm.

The promising results presented in the aforementioned references are the motivation behind the current effort to further examine the mechanical and functional limits of this alloy. The goal is two-fold: first to perform thermochemical tests to an extended number of cycles in isothermal and isobaric modes to quantify the durability of this material for use in longer-life applications, and second to conduct compressive thermomechanical testing using *in situ* synchrotron x-ray diffraction to assess changes in the alloy's internal state and microstructure. Special attention is directed towards quantifying the microstructural reversibility through texture and lattice strains as a function of stress.

2. Material and methods

2.1. Material

The material used in this investigation was part of a larger heat of Ni-rich $Ni_{50.3}Ti_{29.7}Hf_{20}$ (at.%) alloy produced by Flowserve Corporation, Dayton, Ohio. The cast ingots were vacuum

homogenized at 1050 °C for 72 h, followed by extrusion at 900 °C. Mechanical test specimens were machined from the extruded rods (HF202 and HF206) and subjected to an aging treatment of 3 h at 550 ºC followed by furnace cooling to promote the formation of a high density of fine precipitate phase in the microstructure. Various physical and thermomechanical properties of this heat-treated alloy are available in the literature [7-10, 12].

2.2. Microstructural characterization

Microstructure of the extruded and aged material was analyzed using optical microscopy, scanning electron microscopy (SEM), and transmission electron microscopy (TEM) techniques. Samples for optical and SEM were mounted, polished and etched lightly using a mixture of 85% H_2O, 12% HNO_3 and 3% HF (by volume) solution to reveal grain size. Transmission electron microcopy was accomplished using a double tilt holder in a FEI CM200 microscope operating at 200 kV. Samples for TEM were prepared from a 3 mm diameter cylinder that was electro-discharge machined from the extruded and aged material. Disks of ~500 μm thickness were sectioned from this cylinder, mechanically ground to ~130 μm thickness, and then electro-polished using a solution of 20% sulfuric acid and 80% methanol (by volume) cooled to 0 ºC in a Struers Tenupol-5 twin-jet electropolisher. TEM images, diffraction patterns, and energy dispersive spectra were collected and analyzed at room temperature to assess the initial microstructure of the extruded and aged material.

2.3.Ex situ mechanical testing

Ex situ macroscopic experiments were conducted using an MTS servohydraulic load frame. Prior to any testing, cylindrical threaded specimens (5.08 mm in diameter and 15.24 mm in gage

length) were subjected to two stress-free thermal cycles between 30 and 300 °C, performed on the test frame, to relieve any residual stresses resulting from the machining operations. Macroscopic strains were measured using a 12.7 mm gauge, high-temperature extensometer, while heating was controlled using an Ameritherm induction heating system. In all the experiments, a heating rate of 20 °C/min was used, and cooling was achieved through the water-cooled grips. The transformation temperatures: martensite start (M_s), martensite finish (M_f), austenite start (A_s), and austenite finish (A_f) were determined from the stress-free, strain-temperature response and were 142, 126, 155, and 169 ± 2 °C, respectively. Isothermal tests consisted of applying tensile or compressive stresses up to 1 GPa at temperatures from 30 to 300 °C, in strain control at a rate of 1×10^{-4} sec^{-1}. Specimens isothermally deformed and unloaded at room temperature were subsequently (i) re-loaded cyclically to 1 GPa or (ii) heated and cooled once through the phase transformation and re-loaded.

Isobaric testing in compression consisted of thermal cycling between 30 and 300 °C at a constant engineering stress of 0, -100 and -200 MPa for up to 100 cycles and a least 10 thermal cycles at stresses as high as -700 MPa. The loading segment was done at room temperature in load control at a rate of 20 MPa/min. At the end of each series of isobaric strain-temperature tests, specimens were subjected to stress-free thermal cycles to examine the extent of any two-way shape memory effect (TWSME) that may have developed. In this case, TWSME is defined as the ability for the alloys to change and remember shapes on both heating and cooling without an external biasing force. Additionally, the same specimens were then loaded to a different stress level to examine the history dependence of this material.

2.4.In situ diffraction and thermomechanical testing

In situ synchrotron x-ray diffraction experiments were performed at the High Energy Materials Science (HEMS) beamline at the German high-brilliance synchrotron radiation storage ring PETRA III, at DESY, Hamburg. Compression specimens, 5 mm in diameter and 10 mm in length, were deformed using a BÄHR DIL805 dilatometer with a maximum load capability of 25 kN at temperatures up to 1500 °C [14]. Test specimens were inductively heated using a heating rate of 20 °C/min and cooled by flowing argon gas around the sample environment. Diffraction measurements were performed with 100 keV photon energy (λ = 0.12427 Å) in transmission geometry. A beam cross section of 500×500 μm was used with a sample-to-detector distance of 1.572 m. Debye–Scherrer diffraction rings were recorded using a MAR345 image plate detector (345 mm area diameter) with 100 μm pixel size. A schematic of the diffraction setup is shown in Fig. 1.

The *in situ* experiments consisted of load-biased cycling between 30 and 300 °C at constant engineering stress of 0, -100, -200 MPa, and back to the unloaded condition at 0 MPa. At each stress level (2 cycles each), diffraction data was continuously collected during the heating and cooling cycles, which were run at a rate of 20 °C/min. Data processing was performed using the Fit2D software [15], where spectra were integrated over azimuthal increments of 10° into 36 slices for better grain statistics. Variations in peak intensities and peak positions were obtained by fitting individual diffraction peaks with a pseudo-Voigt function. Lattice strains were calculated from the peak shifts using the change in d-spacing where the initial d-spacing was taken in the nominally unloaded condition. The Rietveld method implemented in the Materials Analysis Using Diffraction (MAUD) software was used for texture analysis [16, 17].

3. Results and discussion

3.1 Microstructure – aged material

The microstructure at room temperature was martensitic with an average grain size of approximately 40 μm as revealed by optical microscopy (Fig. 2a). Formation of (Hf,Ti)C was prevented by using a water-cooled copper crucible during melting. However, due to a high affinity of Hf for O_2, formation of HfO_2 particles (size ≤ 1 μm) could not be avoided (Fig. 2b-d). In the TEM, general morphology of the martensite was clearly visible and consisted primarily of two sets of twin variant plates at right angles to each other (Fig. 3a), with small areas of mosaic zig-zag twin structure (Fig. 3b). Each primary set contained variant plates that were related to each other by {011} Type I twins (Fig. 3c). This twinning system has been reported earlier in both Ni-rich [18] and Ti-rich [19] NiTiHf alloys. Within each variant plate fine twins were observed which were identified as $(001)_{B19'}$ compound twins (Fig. 3d). In addition, the aging treatment produced a high density of very fine precipitate phase (size ≤ 15 nm) distributed uniformly throughout the matrix (Fig. 3e). This phase was confirmed to be the "H-phase" (Fig. 3f), as described in detail in recent papers by Yang et al. [12] and Santamarta et al. [6]. It is this fine phase that is responsible for providing high-strength and stability in this alloy system, as described in the remaining sections of this paper.

3.2 Isothermal behavior – tension and compression

The stress-strain-temperature curves for the $Ni_{50.3}Ti_{29.7}Hf_{20}$ alloy in uniaxial tension and compression are shown in Fig. 4. For ease of comparison, the compression curves (Figs. 4c and 5d) were plotted on the first quadrant to directly observe the tension-compression asymmetry and the corresponding differences in strain magnitudes and ensuing strain recoveries. The testing sequence consisted of (*i*) loading to 1 GPa at room temperature (in either tension or

compression), (*ii*) unloading to 0 MPa, (*iii*) heating to 300 °C, and (*iv*) cooling back to room temperature, with the entire sequence repeated for six cycles. For both tensile and compressive loading, room temperature stress-strain responses (Figs. 4a and 4c) were identical after the first cycle (Figs. 4b and 4d) and no plastic strain was observed during the initial loading to 1 GPa. This deformation strain, 3.7% in tension and 2.2% in compression at 1 GPa stress, note the strong asymmetry, is a combination of elastic strain and inelastic martensite variant reorientation/detwinning, but no discernible stress plateau or demarcation between the two mechanisms was observed.

This behavior is further quantified in Fig. 5 by taking the first derivative of stress with respect to strain ($d\sigma/d\varepsilon$). The first derivatives, while a little "noisy," exhibit a non-zero slope along the entire curve during both loading and unloading, indicating the nonlinear stress-strain response. Since this Ni-rich alloy is a two-phase material containing a fine dispersion of second phase precipitates, an increasing externally applied stress is essential in continuing the reorientation and detwinning process. Thus, a distinct plateau is not observed as is the case of some binary, equiatomic NiTi alloys [20]. In addition, this isothermal deformation did not generate any TWSME, likely due to the absence of permanent plastic deformation. While acknowledging the non-linear loading response, application of a best linear-fit through the initial loading and unloading portions of curves in Figs. 4a and 4c (approximately through 100 MPa), results in an estimated range for the "apparent" Young's modulus of 58–61 GPa in tension, and 61–75 GPa in compression over the initial loading and unloading sections of the stress-strain curves.

Cyclic isothermal tests were also conducted at room temperature in tension and compression as shown in Fig. 6. Specimens were cyclically loaded to 1 GPa and unloaded (repeated for a

maximum of 100 cycles) to examine strain ratcheting and instabilities if any. Two specimens tested in tension both failed at the threads during the 72^{nd} and 85^{th} cycle. Cyclic stress-strain data in tension for the sample that failed at 72 cycles is shown in Fig. 6a. An image of the actual test sample that fractured is shown in Fig. 6b. It should be noted that no localized deformation or necking was observed in the samples' gauge sections, and failure occurred due to defects introduced during thread machining operations at the high stress concentration located at the thread roots. On the other hand, samples tested in compression (using the same geometry), did not fracture and the cyclic response is shown in Fig. 6c.

Irrespective of the testing mode, the strain evolution exhibited similar behavior, i.e., the strain at the loaded condition (±1 GPa) shifted $^{T}0.1$ and $^{C}0.08\%$ towards zero with cycling, and the strain values at 0 MPa shifted $^{T}0.23$ and $^{C}0.12\%$ towards higher strain with cycling, where superscripts 'T' and 'C' refer to tension and compression, respectively. This indicates that the stress-strain slopes become steeper with increasing number of cycles, which is attributed to stabilization of the favored martensite variants. Aside from these small strain shifts, the cyclic loops were repeatable with no accumulation of plastic strain. Post thermal cycling at 0 MPa of the undeformed and the isothermally cycled compression samples (Fig. 7a and 7b, respectively) showed no difference in strain-temperature response. Further, this response was extended up to 100 cycles (not shown in Fig. 7b) and no TWSME was observed; the material performing similar to an undeformed 'virgin' material with no prior history.

Additional isothermal tests at temperatures between 30 and 260 °C were conducted to assess the effect of temperature on the mechanical response and stress-induced transformation behavior of this material. The results for tensile loading are shown in Fig. 8. These tests were performed in series, where after each load-unload cycle (Figs. 8a and 8c) samples were heated and cooled

once through the phase transformation at 0 MPa (Figs. 8b and 8d), before heating to the next test temperature and re-loading. Below the A_s temperature (Figs. 8a and 8b), the stress-strain curves exhibited a lower hardening rate with increasing temperature (Fig. 8a) and accumulation of ~0.2% total unrecovered strain after five load-unload cycles at temperatures between 30 and 140 °C. This would be expected since the yield onset is known to decrease with increasing test temperature as was shown for other SMAs [21-23], which in this case resulted in minuscule although permanent deformation. Above the A_f temperature (Figs. 8c and 8d), the stress-strain curves exhibited an initial linear elastic loading of the austenite phase followed by a stress plateau associated with the stress-induced martensitic (SIM) transformation. Note that while the curves in Fig. 8a were limited to 1 GPa, the curves in Fig. 8c were limited to 3% strain, since the primarily interest was in the superelastic response in this case. The unrecovered strains were less than 0.02% (almost negligible) for samples deformed at 200 and 220 °C, 0.08% at 240 °C and 0.18% at 260 °C. The onset stress for the SIM estimated using the 0.2% offset stress, increased with increasing test temperature consistent with a Clausius-Clapeyron relationship. The average elastic moduli for the austenite phase measured above A_f were 75 GPa in tension (from Fig. 8c) and 80 GPa in compression (curves not shown).

A small TWSME was introduced, illustrated in Figs. 8b and 8d, as the material started to accumulate unrecovered strains. Loading below A_s or above A_f where the deformation was not fully reversible (e.g., 140 or 260 °C test temperatures) is expected to result in the formation of internal stress fields that can emerge from a number of sources including dislocation arrays. However, the TWSME magnitude was less than 0.2% when originated through isothermal deformation, which is an order of magnitude less than that observed in binary NiTi under comparable conditions [20].

3.3 Isobaric behavior–compression

Isobaric thermal cycles in compression are shown in Fig. 9. For all testing, an upper cycle temperature of 300 °C (130 ºC above A_f) was used to ensure complete phase transformation under load. Two cases were considered to examine the history dependence of this alloy: the first case (labeled a-1 through d-1) consisted of series thermal cycling under 0 MPa, -100 MPa, -200 MPa, and back to 0 MPa in this order. The second case (labeled a-2 through d-2) consisted of series thermal cycling of a new sample under 0 MPa, -200 MPa, -100 MPa, and back to 0 MPa, noting that the second and third loading sequence was reversed in the second case as compared to that in the first case. At each condition, 100 cycles were performed totaling 400 cycles on each specimen.

From the stress-free strain-temperature response, the martensite and austenite coefficients of thermal expansion (CTE) were measured to be 7×10^{-6}/ºC and 11×10^{-6}/ºC, respectively. The transformation strain of 0.17% associated with the undeformed sample (Fig. 9(a-1)) is due to the combined Bain strain and lattice invariant shear, in addition to a minor texture that developed during the hot extrusion process [7].

On loading to -100 MPa (Fig. 9 (b-1)), a characteristic transient response was observed on the first heating cycle, followed by a larger strain buildup on cooling. With the accumulation of cycles, the end-strain in the austenite phase remained nearly constant over the 100 cycles, while the end-strain in the martensite evolved to higher values as more detwinning/reorientation of the martensite phase occurred. This evolution resulted in a growing actuation strain, when calculated by taking the difference between the martensite and austenite true end-strains. Note that when referring to the transformation strain as opposed to actuation strain, the former is calculated as

the relative true strain between the austenite finish and austenite start intersections as demonstrated in [1], which in this case also follows the same trend as the actuation strain.

At the end of thermal cycling at -100 MPa stress, the compressive stress was increased to -200 MPa (Fig. 9 (c-1)), and an additional 100 thermomechanical cycles followed. Similar behavior can be observed with regard to the first transient heating curve and the evolution of the martensite end-strain, although much smaller evolution than the previous stress value was attained. The specimen was then unloaded to 0 MPa and thermally cycled (Fig. 9 (d-1)), where all the strains that were generated throughout the isobaric cycling were recovered on the first heating cycle. The end-strain in the austenite phase was identical to the initial 0 MPa thermal cycle (Fig. 9 (a-1)), but the end-strains in the martensite exhibited a different behavior displaying a narrower transformation loop. Nonetheless, there was no TWSME developed at the end of cycling in this scenario.

Similar observations were made from the second case shown in Figs. 9 (a-2) through 9 (d-2). In this case, the -200 MPa stress was applied first (Fig. 9 (c-2) before the -100 MPa stress. The results in Fig. 9 (c-2) indicate that strain ratcheting is taking place at both phases, but higher evolution occurs in the martensite phase. Once the stress was reduced to -100 MPa, the thermomechanical response was stable without any evolution, though all SME values were similar to those shown in Fig. 9 (b-1). Overall, comparing the two cases, the strain-temperature responses show similar behavior indicating that except for stabilization in evolutionary behavior at -100 MPa the shape memory response is essentially history independent under this range of stresses due to the lack of permanent deformation. Furthermore, in either case, there was no TWSME present after cycling with the current load and temperature conditions.

Additional isobaric tests were performed at higher stresses followed by stress free thermal cycles (Fig. 10). At each condition, the sample was thermomechanically cycled ten times under load, followed by ten stress-free thermal cycles. Then the same sample was reloaded to the next stress level and cycled again. Strain evolution (strain ratcheting at both phases), while very small in all cases, was noticeable starting at stresses of -500 MPa and higher, and at those stresses, the TWSME started to appear and grow with higher loads as indicated in Fig. 10. In this testing configuration, a maximum TWSME of 0.63% was obtained post cycling to -700 MPa. These instabilities are attributed to plastic deformation, most likely in the austenite phase, and the possibility of retained martensite as was observed in binary NiTi [24] and NiTiPd alloys [25]. However, relatively speaking, the load stability of this alloy is highly remarkable, since the strain evolution is over an order of magnitude less at stress levels twice as high as observed in other shape memory alloys [24, 25]. In addition, a significantly reduced TWSME due to thermomechanical cycling was observed compared to that developed in other NiTi-based systems at a fraction of the stress [26].

A summary of the actuation strain is shown in Fig. 11. Both the actuation strains on the first and last cycle are plotted for comparison. It was found that only a small variation from the first to the last cycle was obtained, and the actuation strain appeared to reach a limit at a maximum of 2.65% in compression.

The stress dependence of the transformation temperatures is shown in Fig. 12. From 0 to -200 MPa, the temperatures follow a non-linear behavior with an initial shift towards lower temperatures followed by near constant behavior as the stress increases. At stresses higher than -200 MPa, the transformation temperatures follow an expected linear trend and shift to higher

temperatures with increasing stress. Linear correlations were fit through the stress-temperature data at stresses higher than -200 MPa as shown in Fig. 12.

3.4 In situ synchrotron x-ray diffraction results

Analogous to the isobaric *ex situ* testing presented above, *in situ* testing was conducted to mimic the loading sequence of the first case in Fig. 9, but for only 2 cycles at each load step. The corresponding displacement-temperature response is presented in Fig. 13. After two cycles at 0, -100 and -200 MPa, successively, the sample was unloaded to 0 MPa and heated once through the phase transformation where all the strains were recovered. Diffraction spectra corresponding to the second cycle of each load step of Fig. 13 are shown in Fig. 14 as the sample undergoes a phase transformation from martensite to austenite during heating. These patterns were obtained by integrating the full diffraction ring over the azimuthal angle (ψ) defined in Fig. 1. Existing phases were previously identified [7] as B2 austenite at high temperature and B19' martensite at lower temperature. The results indicate complete transformation with thermal cycling under all conditions shown in Fig. 13. There is no evidence of retained martensite above the bulk A_f, even under an isobaric stress of -200 MPa, in contrast to binary NiTi where residual martensite is noted even when cycling under stress free conditions [21]. In addition, there is no indication of residual austenite below the measured M_f temperature. The transformation is complete in both directions at the representative martensite and austenite finish temperatures.

Normalized intensities (I/I_0) of select martensite peaks at room temperature and austenite peaks at 300 °C were determined as a function of the azimuthal angle integrated over 10° ψ segments, where $\psi = 0°$ is the compression axis. Intensity data was plotted in normalized scale to compare the intensity changes with cycling and changing macroscopic stresses. Fig. 15 contains

several martensite peaks plotted on radial 10° ψ segments. The intensities of some of the martensite planes, particularly along the loading direction, varies as the sample was cycled under load, indicative of the formation and reorientation of preferred martensite variants capable of accommodating the applied strain that takes place on constrained cooling. The intensities further change from -100 to -200 MPa, which is macroscopically manifested by additional transformation strains as shown in Figs. 9 and 14. Microstructurally, the $(011)_M$, $(111)_M$ and $(103)_M$ lattice planes preferentially orient with the loading axis, while the $(110)_M$ and $(030)_M$ planes display only a slight variation in intensity. Once the load was removed, the intensities of the individual lattice planes return to their initial values at 0 MPa before cycling, consistent with the fully reversible macroscopic observations.

In a similar analysis, the normalized intensities of B2 austenite at 300 °C are shown in Fig. 16. As opposed to the changing intensities of the martensite phase, the austenite intensities did not vary with cycling or with changing load. This unchanging austenitic texture is also an indication that no new or additional deformation mechanisms ensue from thermal cycling under the current conditions and that the underlying microstructure has not been affected by prior history. These microstructural results are fully consistent with the lack of plastic deformation under the current conditions and help explain why the strains generated during the isobaric thermal cycling were fully reversible.

Lattice strains for a select family of planes were calculated using $\varepsilon_{hkl} = \Delta d/d_0$, where d_0 is the initial d-spacing of the starting material at 0 MPa macroscopic stress. Lattice strains in the martensite phase, shown in Fig. 17, exhibited an anisotropy associated with the low symmetry monoclinic phase. At $\psi = 0$, which corresponds to the loading axis, some lattice planes exhibited strains as high as -1.6% in the case of the $(030)_M$ planes, while others developed an order of

magnitude less strain such as the $(110)_M$ planes. Moreover, there is large deviation in strain magnitude over different azimuthal angles as illustrated by the $(111)_M$ planes. Regardless of the initial anisotropy or strain heterogeneity, all the lattice strains were recovered after load removal consistent with the macroscopic findings presented in previous sections.

In contrast to the martensite phase, lattice strains for the austenite phase are isotropic in nature as shown in Fig. 18. Nevertheless, similar observations were made regarding the strain reversibility after load removal with no residual lattice strain observed. The lattice strain reversibility is also an indication of the lack of internal/residual strains that would otherwise help drive the TWSME. Without any internal stresses, the material, as demonstrated macroscopically, exhibited no TWSME under the test conditions shown in Fig 14.

4. Conclusions

Basic mechanical, thermomechanical, and microstructural behaviors of the precipitation strengthened, Ni-rich $Ni_{50.3}Ti_{29.7}Hf_{20}$ high temperature shape memory alloy were investigated in isothermal and isobaric conditions. From the *ex situ* macroscopic and *in situ* synchrotron x-ray diffraction results, the following conclusions can be made:

1. Isothermal deformation of the martensite phase at room temperature resulted in no plastic deformation or other irrecoverable strains when tested to 1 GPa uniaxial tensile and compressive stresses. In addition, extended cycling at this stress level did not introduce any permanent deformation and all strains were transformation related and recovered upon heating through the phase transformation.
2. A near-perfect superelastic behavior, without generation of significant residual strain, was obtained at temperatures between 180 and 220 °C, with recoverable strains in the order of 3%

upon unloading. Plastic deformation was apparent only at temperatures higher than 220 °C, resulting in a small ~0.2% TWSME.

3. Isothermal deformation in either the martensite or austenite phases did not yield a large and stable TWSME, mainly due to lack of internal/residual stress fields, since plastic deformation was not introduced under the test conditions investigated.
4. Dimensionally stable responses were observed during isobaric thermal cycling, with no prior training requirement. Maximum actuation strains of approximately 2.65% were achieved in compression. Finally, stability was also manifested in the microstructure, which reverted back to its original state after extended cycling at 200 MPa, as demonstrated through synchrotron x-ray diffraction measurements.
5. *In situ* diffraction spectra, collected during isobaric thermal cycling, revealed preferentially oriented martensite variants that revert back to the original microstructure upon load removal. No texture changes were observed in the austenite phase and no evidence for plastic deformation was detected in the spectra when cycling with stresses up to -200 MPa. Similarly, measured lattice strains were found to fully recover after load removal and stress-free thermal cycling, leaving no residual strains behind. These findings are consistent with the lack of macroscopic residual strains and the absence of TWSME.
6. Isobaric thermal cycling at high stresses, exceeding 500 MPa, resulted in slight dimensional instabilities and a maximum TWSME of 0.6% after cycling at -700 MPa. Isobarically, a higher TWSME was obtained compared to the introduction of isothermal deformation, but neither case produced significant TWSME in this alloy.

Acknowledgment

Funding from the NASA Fundamental Aeronautics Program, Aeronautical Sciences Project is gratefully acknowledged. The authors thank A. Stark for technical support with the diffraction experiments. This work has benefited from the use of the HEMS beamline at the German high-brilliance synchrotron radiation storage ring PETRA III on DESY.

References

[1] G.S. Bigelow, S.A. Padula, II, A. Garg, D. Gaydosh, R.D. Noebe, Characterization of Ternary NiTiPd High-Temperature Shape-Memory Alloys under Load-Biased Thermal Cycling, Metall. Mater. Trans. A, 41 (2010) 3065-3079.

[2] L. Kovarik, F. Yang, A. Garg, D. Diercks, M. Kaufman, R.D. Noebe, M.J. Mills, Structural analysis of a new precipitate phase in high-temperature TiNiPt shape memory alloys, Acta Mater., 58 (2010) 4660-4673.

[3] L. Kovarik, F. Yang, R.D. Noebe, M.J. Mills, High Resolution Microscopy Analysis of a New Precipitate Phase in the High-Temperature Shape Memory Alloy $Ni_{30}Pt_{20}Ti_{50}$, Microscopy and Microanalysis, 15 (2009) 1402-1403.

[4] R. Noebe, S. Draper, D. Gaydosh, A. Garg, B. Lerch., N. Penney, G. Bigelow, S. Padula, J. Brown, Effect of Thermomechanical Processing on the Microstructure, Properties, and Work Behavior of a $Ti_{50.5}Ni_{29.5}Pt_{20}$ High-Temperature Shape Memory Alloy, in: SMST 2006: Proceedings of the International Conference on Shape Memory and Superelastic Technologies, Pacific Grove, CA, 2008, pp. 409-426.

[5] A. Evirgen, I. Karaman, R.D. Noebe, R. Santamarta, J. Pons, Effect of precipitation on the microstructure and the shape memory response of the Ni50.3Ti29.7Zr20 high temperature shape memory alloy, Scr. Mater., 69 (2013) 354-357.

[6] R. Santamarta, R. Arróyave, J. Pons, A. Evirgen, I. Karaman, H.E. Karaca, R.D. Noebe, TEM study of structural and microstructural characteristics of a precipitate phase in Ni-rich Ni–Ti–Hf and Ni–Ti–Zr shape memory alloys, Acta Mater., 61 (2013) 6191-6206.

[7] O. Benafan, R.D. Noebe, S.A. Padula II, R. Vaidyanathan, Microstructural Response During Isothermal and Isobaric Loading of a Precipitation-Strengthened Ni-29.7Ti-20Hf High-Temperature Shape Memory Alloy, Metall. Mater. Trans. A, 43A (2012) 4539-4552.

[8] D.R. Coughlin, P.J. Phillips, G.S. Bigelow, A. Garg, R.D. Noebe, M.J. Mills, Characterization of the microstructure and mechanical properties of a 50.3Ni–29.7Ti–20Hf shape memory alloy, Scr. Mater., 67 (2012) 112-115.

[9] H.E. Karaca, S.M. Saghaian, B. Basaran, G.S. Bigelow, R.D. Noebe, Y.I. Chumlyakov, Compressive response of nickel-rich NiTiHf high-temperature shape memory single crystals along the [1 1 1] orientation, Scr. Mater., 65 (2011) 577-580.

[10] G.S. Bigelow, A. Garg, S.A. Padula Ii, D.J. Gaydosh, R.D. Noebe, Load-biased shape-memory and superelastic properties of a precipitation strengthened high-temperature $Ni_{50.3}Ti_{29.7}Hf_{20}$ alloy, Scr. Mater., 64 (2011) 725-728.

[11] J. Ma, I. Karaman, R.D. Noebe, High temperature shape memory alloys, Int. Mater. Rev., 55 (2010) 257-315.

[12] F. Yang, D.R. Coughlin, P.J. Phillips, L. Yang, A. Devaraj, L. Kovarik, R.D. Noebe, M.J. Mills, Structure analysis of a precipitate phase in an Ni-rich high-temperature NiTiHf shape memory alloy, Acta Mater., 61 (2013) 3335-3346.
[13] M. Moshref-Javadi, S.H. Seyedein, M.T. Salehi, M.R. Aboutalebi, Age-induced multi-stage transformation in a Ni-rich NiTiHf alloy, Acta Mater., 61 (2013) 2583-2594.
[14] http://thermophysical.tainstruments.com/instruments/dilatometers/dil-805ad-quenching-and-deformation-dilatometer/ (2013), in.
[15] A.P. Hammersley, ESRF internal report, ESRF98HA01T, FIT 2D V9.129 reference manual V3.1, (1998).
[16] L. Lutterotti, S. Matthies, H.-R. Wenk, A.J. Schultz, J.W. Richardson, Texture and structure analysis of deformed limestone from neutron diffraction spectra, J. Appl. Phys., 81 (1997) 594-600.
[17] G. Ischia, H.-R. Wenk, L. Lutterotti, F. Berberich, Quantitative Rietveld texture analysis of zirconium from single synchrotron diffraction images, J. Appl. Cryst., 38 (2005) 377-380.
[18] A. Garg, G. Bigelow, S. Saghaian, Y. Chumlyakov, H. Karaca, R.D. Noebe, Martensitic Transformation in a High-Temperature High-Strength <001> Single Crystal NiTiHf Shape Memory Alloy, in: Proc. IMC-17, International Microscopy Congress (IMC17), Paper M8.46, Rio de Janeiro, Brazil, 2010.
[19] X.D. Han, W.H. Zou, R. Wang, Z. Zhang, D.Z. Yang, Structure and substructure of martensite in a $Ti_{36.5}Ni_{48.5}Hf_{15}$ high temperature shape memory alloy, Acta Mater., 44 (1996) 3711-3721.
[20] O. Benafan, S.A. Padula II, R.D. Noebe, T.A. Sisneros, R. Vaidyanathan, Role of B19' martensite deformation in stabilizing two-way shape memory behavior in NiTi, J. Appl. Phys., 112 (2012) 093510.
[21] O. Benafan, R.D. Noebe, S.A. Padula II, D.J. Gaydosh, B.A. Lerch, A. Garg, G.S. Bigelow, K. An, R. Vaidyanathan, Temperature-dependent behavior of a polycrystalline NiTi shape memory alloy around the transformation regime, Scr. Mater., 68 (2013) 571–574.
[22] A. Stebner, S. Padula, R. Noebe, B. Lerch, D. Quinn, Development, Characterization, and Design Considerations of $Ni_{19.5}Ti_{50.5}Pd_{25}Pt_5$ High-temperature Shape Memory Alloy Helical Actuators, Journal of Intelligent Material Systems and Structures, 20 (2009) 2107-2126.
[23] S. Padula, G. Bigelow, R. Noebe, D. Gyadosh, A. Garg, Challenges and Progress in the Development of High-Temperature Shape Memory Alloys Based on NiTiX Compositions for High-Force Actuator Applications, in: SMST 2006: Proceedings of the International Conference on Shape Memory and Superelastic Technologies, Pacific Grove, CA, 2008, pp. 787-802.
[24] S.A. Padula, S. Qiu, D. J. Gaydosh, R. Noebe, Glen Bigelow, A. Garg, R. Vaidyanathan, Effect of Upper-Cycle Temperature on the Load-biased, Strain-Temperature Response of NiTi, Metall. Mater. Trans. A, 43 (2011) 4610-4621.
[25] S. Qiu, in, Ph.D. dissertation, University of Central Florida, Orlando, FL, 2010.
[26] K.C. Atli, I. Karaman, R.D. Noebe, D. Gaydosh, The effect of training on two-way shape memory effect of binary NiTi and NiTi based ternary high temperature shape memory alloys, Mater. Sci. Eng., A, 560 (2013) 653-666.

Figures:

Fig. 1. Schematic illustration of the experimental diffraction setup.

Fig. 2. Optical micrograph showing grain size and martensite twins, (b) SEM showing HfO_2 particles in a martensite matrix, (c) EDS of the white particles showing enrichment of Hf and O_2, (d) EDS of nearby matrix for comparison to (c).

Fig. 3. (a,b) TEM showing general morphology of the twin variants, (c) analysis of twin variant plates within a set, (d) analysis of twins within a variant plate, (e) dark-field image showing fine precipitate phase, (f) confirmation of precipitate phase as H-phase. Projection of common planes is marked by red lines in (c,d).

Fig. 4. Stress-strain-temperature curves for the $Ni_{50.3}Ti_{29.7}Hf_{20}$ alloy in uniaxial tension and compression. (a) Tensile stress-strain behavior, and (b) corresponding unconstrained thermal recovery after each tensile deformation in (a), (c) compressive stress-strain behavior, and (d) corresponding unconstrained thermal recovery after each compressive deformation in (c).

Fig. 5. First derivative of stress with respect to strain ($d\sigma/d\varepsilon$) for (a) tension and (b) compression loading.

Fig. 6. Room temperature cyclic stress-strain responses of $Ni_{50.3}Ti_{29.7}Hf_{20}$ in (a) tension and (c) compression. The inset (b) indicates the specimen fracture site at the 72^{nd} cycle in tension.

Fig. 7. No-load strain-temperature response for $Ni_{50.3}Ti_{29.7}Hf_{20}$ showing ten thermal cycles (at 0 MPa) for (a) an undeformed 'virgin' sample and (b) after deformation according to Fig. 4b.

Fig. 8. Stress-strain-temperature curves for the $Ni_{50.3}Ti_{29.7}Hf_{20}$ alloy in uniaxial tension at different temperatures. (a) Stress-strain behavior below A_s, and (b) corresponding unconstrained thermal recovery after each deformation sequence in (a) and, (c) stress-strain behavior above A_f, and (d) corresponding unconstrained thermal recovery after each deformation sequence in (c).

Fig. 9. Isobaric strain-temperature response of the $Ni_{50.3}Ti_{29.7}Hf_{20}$ for different loading histories, i.e., a-1 thru d-1 and a-2 thru d-2. The constant stress level and cycle number are indicated for each set of curves.

Fig. 10. Isobaric strain-temperature response of the $Ni_{50.3}Ti_{29.7}Hf_{20}$ alloy at different stresses. After each ten isobaric thermal cycles at a constant stress, ten stress-free thermal cycles were applied before incrementing to the next load.

Fig. 11. Compressive actuation strain summary for the $Ni_{50.3}Ti_{29.7}Hf_{20}$ alloy for the first cycle (solid symbols), and for the last cycle (open symbols).

Fig. 12. Transformation temperatures for the $Ni_{50.3}Ti_{29.7}Hf_{20}$ alloy as function of compressive stress.

Fig. 13. *In situ* isobaric displacement-temperature response of the $Ni_{50.3}Ti_{29.7}Hf_{20}$ alloy at different stresses.

Fig. 14. *In situ* synchrotron x-ray diffraction spectra corresponding to the second heating cycle of each load step of Fig. 13. These spectra show the martensite to austenite transition on heating.

Fig. 15. Normalized diffraction intensities (I/I_0) of select martensite peaks at room temperature as a function of the azimuthal angle integrated over 10° ψ segments, where ψ = 0° is the compression axis.

Fig. 16. Normalized diffraction intensities (I/I_0) of select austenite peaks at 300 °C as a function of the azimuthal angle integrated over 10° ψ segments, where ψ = 0° is the compression axis.

Fig. 17. Lattice strains for a select family of planes in the martensite phase at room temperature as a function of the azimuthal angle integrated over 10° ψ segments.

Fig. 18. Lattice strains for a select family of planes in the austenite phase at 300 °C as a function of the azimuthal angle integrated over 10° ψ segments.

Fig. 1

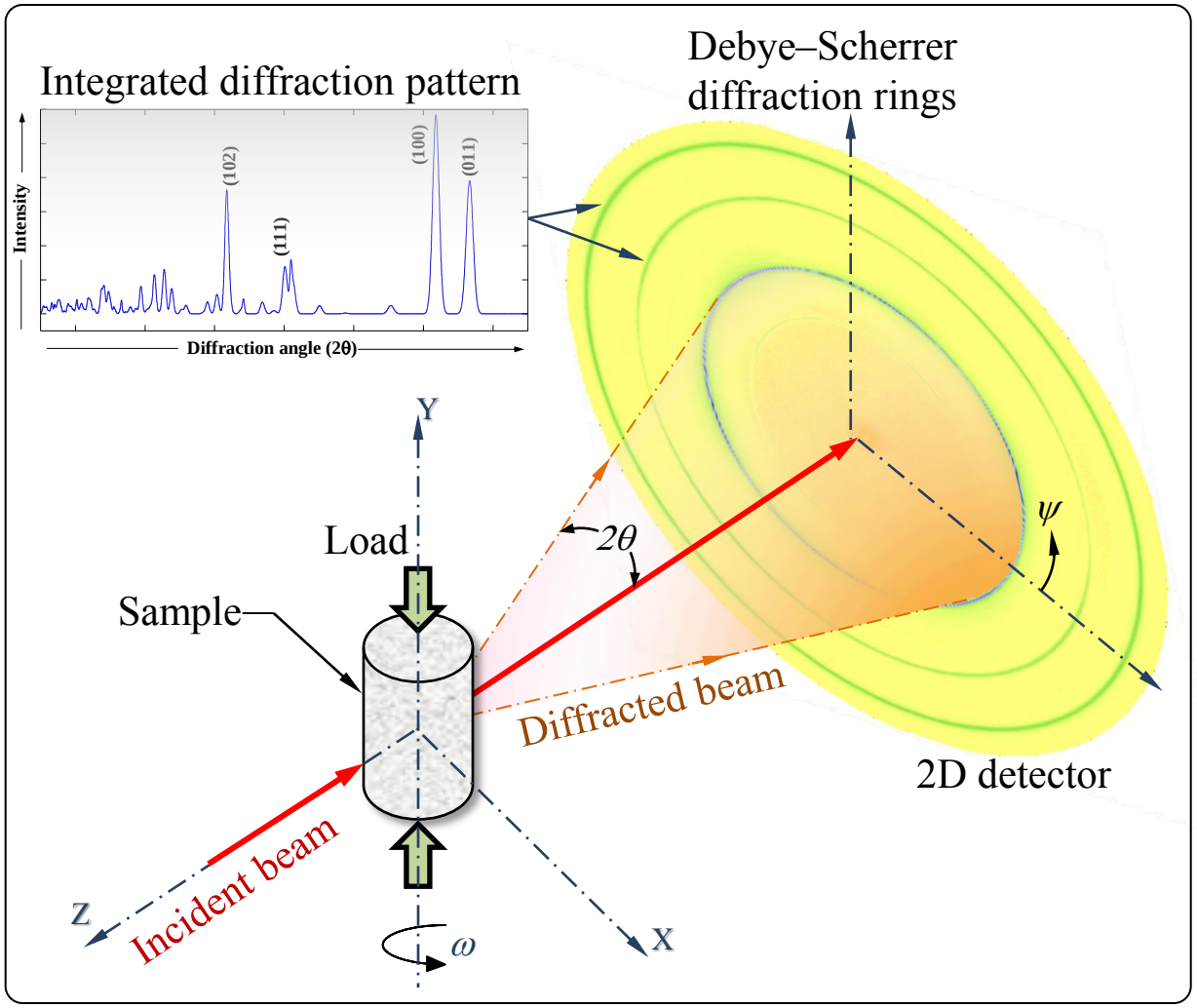
Integrated diffraction pattern
Intensity
(102)
(111)
(100)
(011)
Diffraction angle (2θ)
Debye–Scherrer
diffraction rings
Y
Load
Sample
2θ
ψ
Diffracted beam
2D detector
Incident beam
Z
X
ω

Fig. 2

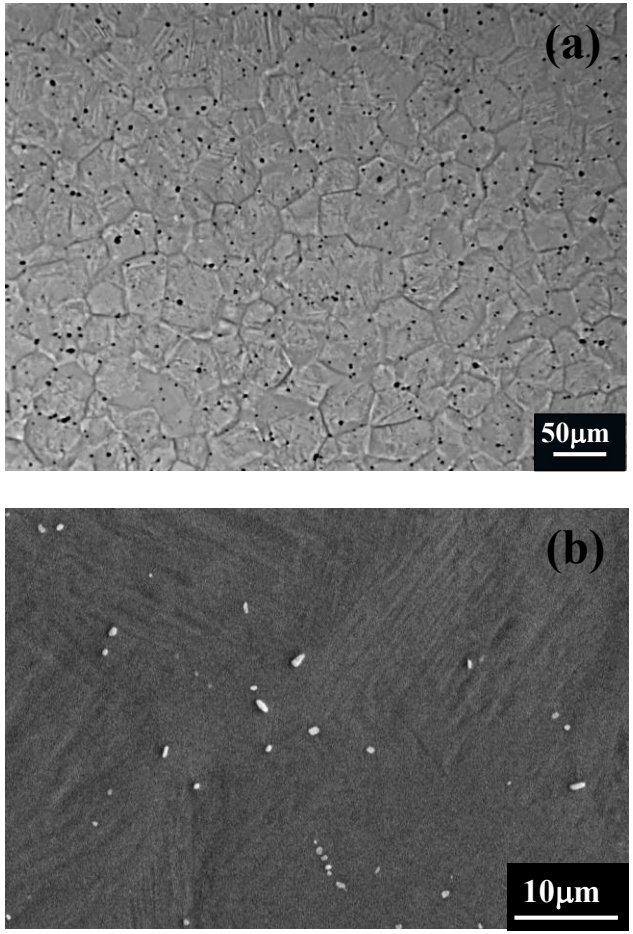
(a)
50μm
(b)
10μm
(c)
EDS: Particle
HfM
OK
TiK
NiK
HfL
HfL
(d)
EDS: Matrix
HfM
NiL
TiK
NiK
HfL

Fig. 3

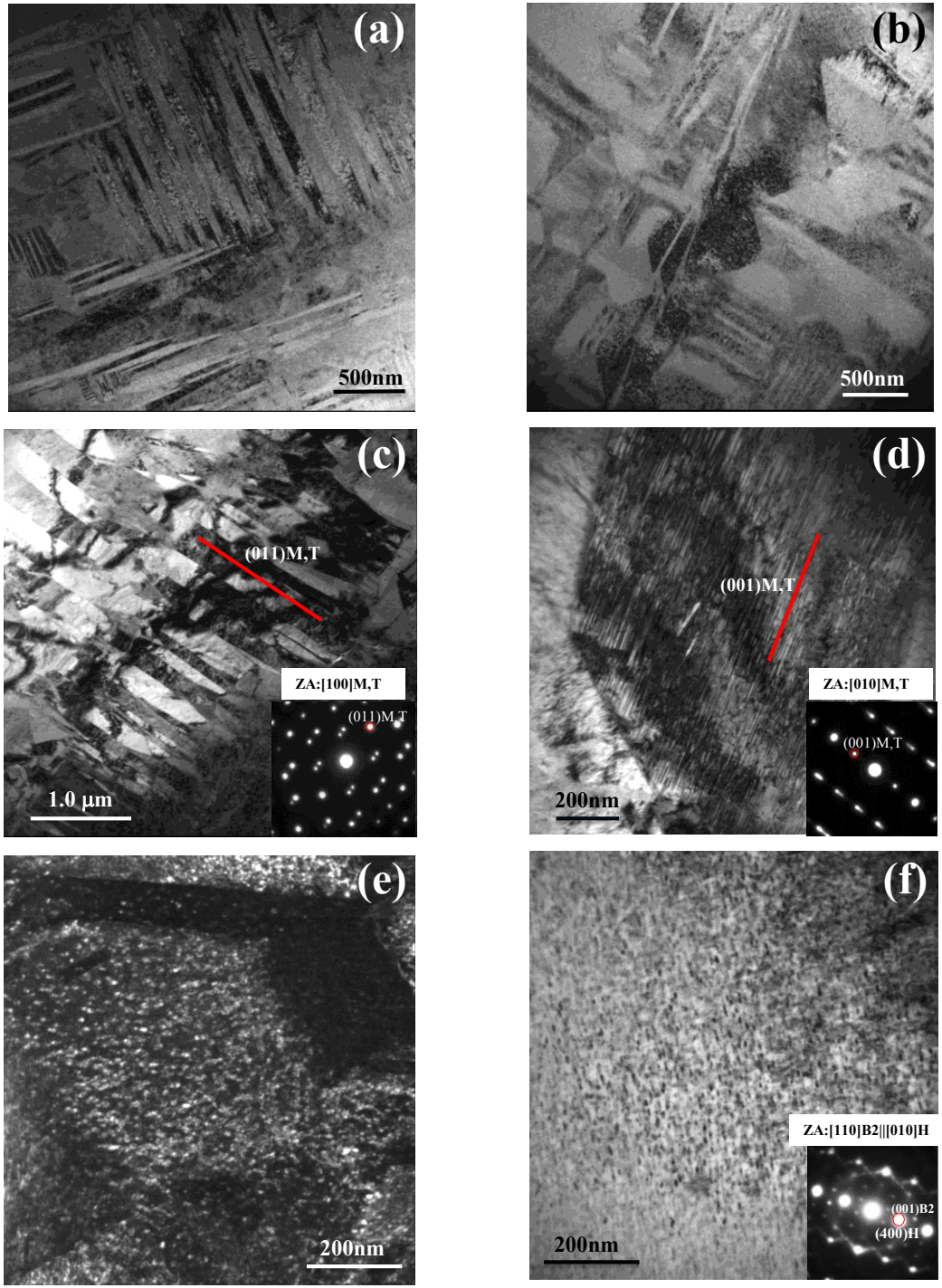
(a)
500nm
(b)
500nm
(c)
(011)M,T
ZA:[100]M,T
(011)M,T
1.0 μm
(d)
(001)M,T
ZA:[010]M,T
(001)M,T
200nm
(e)
200nm
(f)
ZA:[110]B2||[010]H
(001)B2
(400)H
200nm

Fig. 4

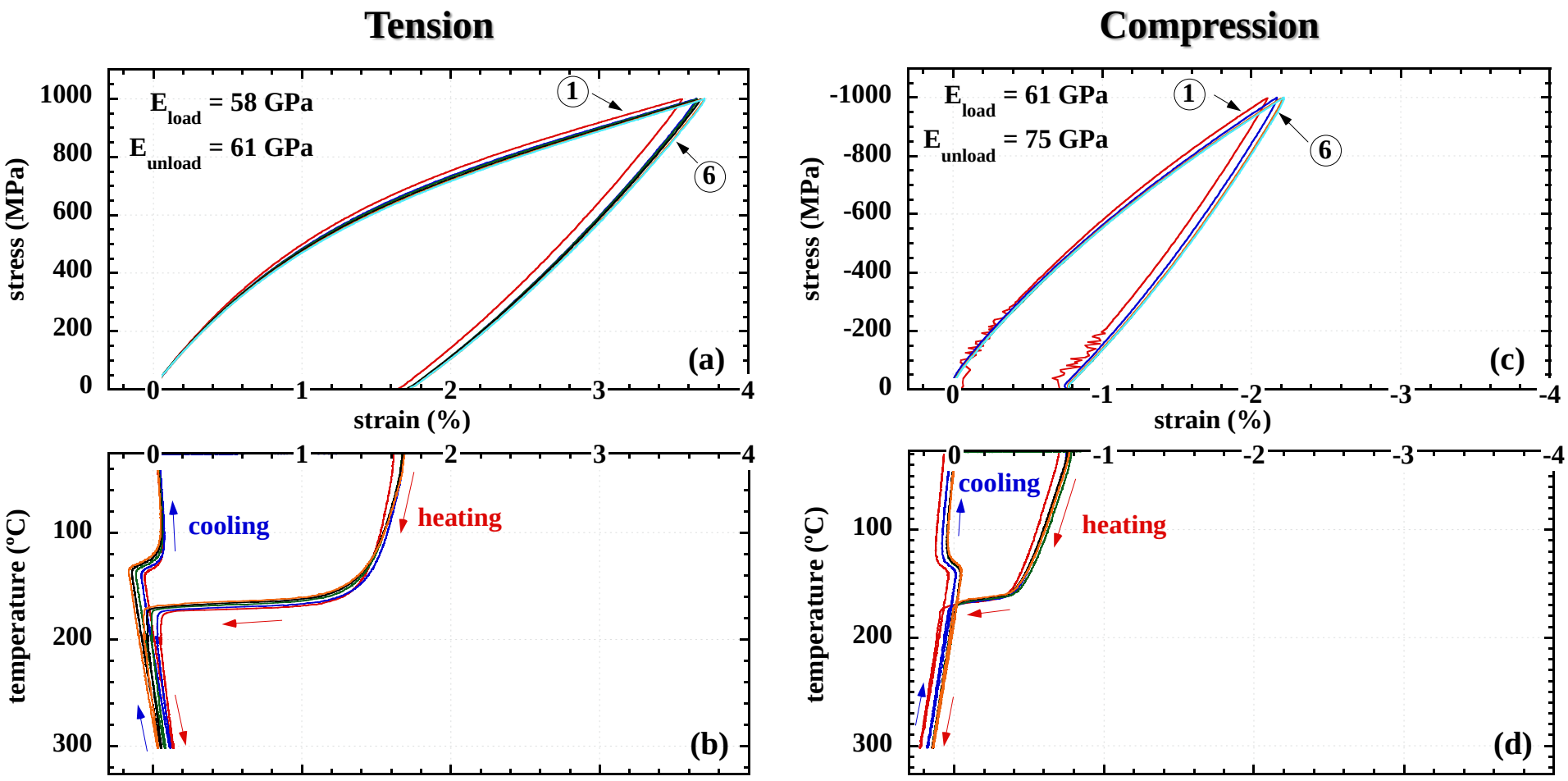
Tension
Compression
E load = 58 GPa
E unload = 61 GPa
E load = 61 GPa
E unload = 75 GPa
1
6
stress (MPa)
strain (%)
cooling
heating
temperature (°C)
(a)
(b)
(c)
(d)

Fig. 5

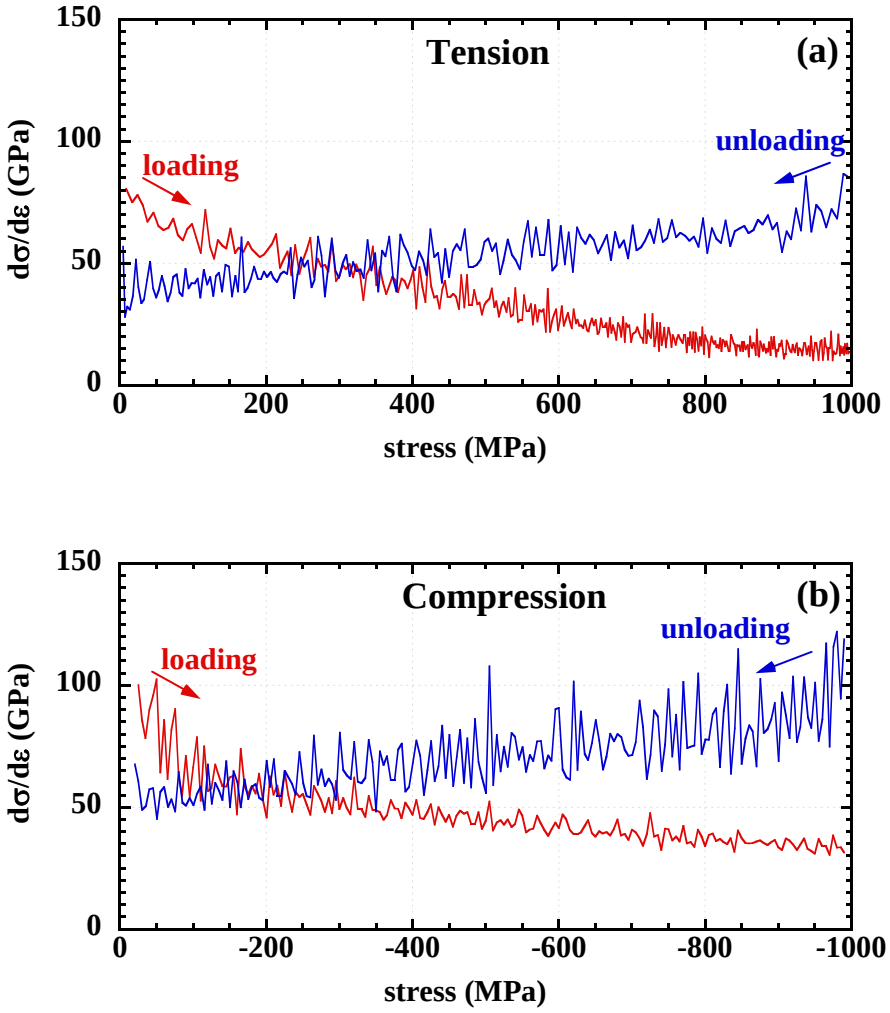
Tension
(a)
loading
unloading
dσ/dε (GPa)
stress (MPa)
0
50
100
150
0
200
400
600
800
1000
Compression
(b)
loading
unloading
dσ/dε (GPa)
stress (MPa)
0
50
100
150
0
-200
-400
-600
-800
-1000

Fig. 6

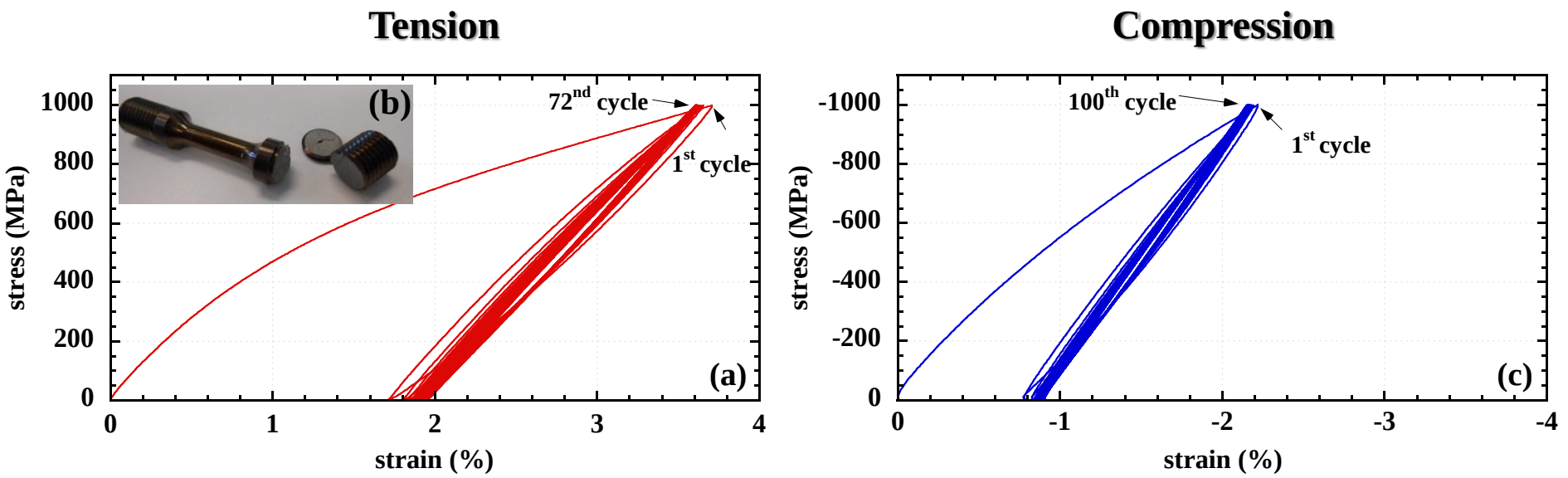
Tension
Compression
(a)
(b)
(c)
72nd cycle
1st cycle
100th cycle
1st cycle
stress (MPa)
strain (%)
1000
800
600
400
200
0
-1000
-800
-600
-400
-200
0
1
2
3
4
-1
-2
-3
-4

Fig. 7

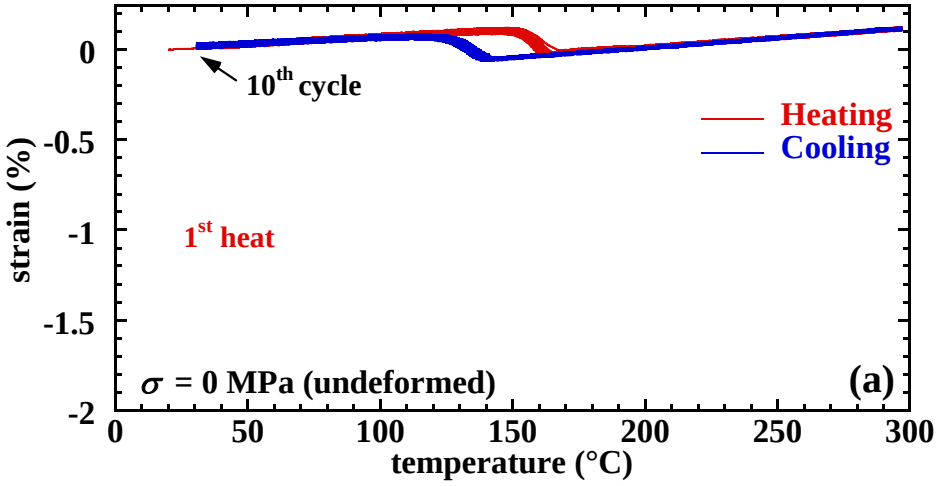
0
-0.5
-1
-1.5
-2
strain (%)
0
50
100
150
200
250
300
temperature (°C)
10th cycle
Heating
Cooling
1st heat
σ = 0 MPa (undeformed)
(a)

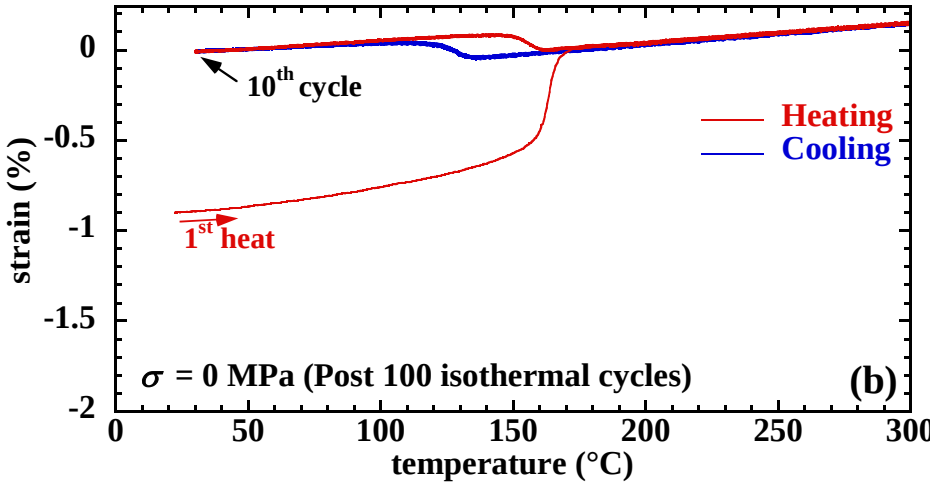
0
-0.5
-1
-1.5
-2
strain (%)
0
50
100
150
200
250
300
temperature (°C)
10th cycle
Heating
Cooling
1st heat
σ = 0 MPa (Post 100 isothermal cycles)
(b)

Fig. 8

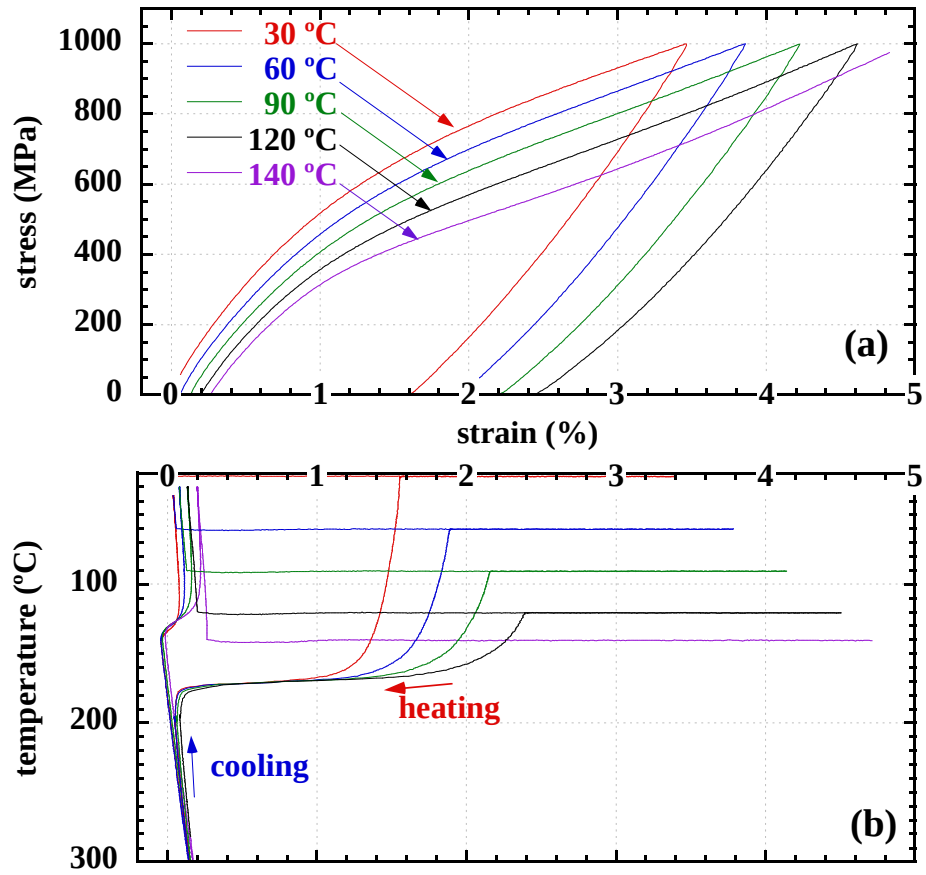
30 °C
60 °C
90 °C
120 °C
140 °C
stress (MPa)
strain (%)
(a)

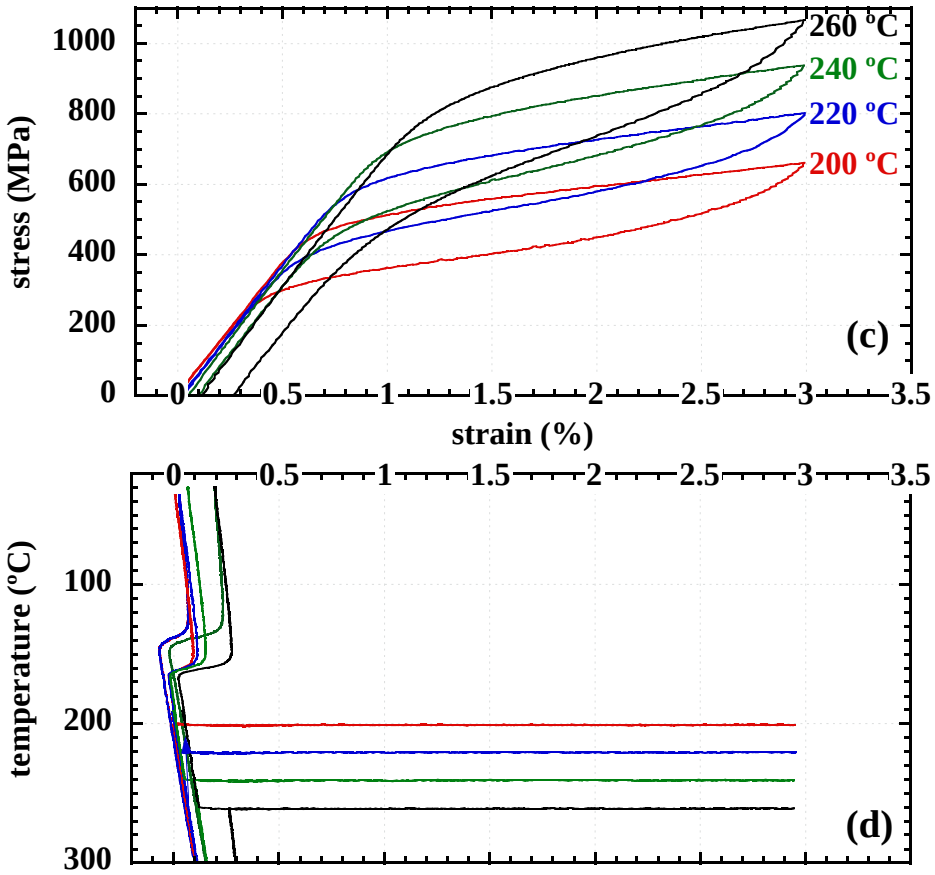
260 °C
240 °C
220 °C
200 °C
stress (MPa)
strain (%)
(c)

temperature (°C)
heating
cooling
(b)

temperature (°C)
(d)

Fig. 9

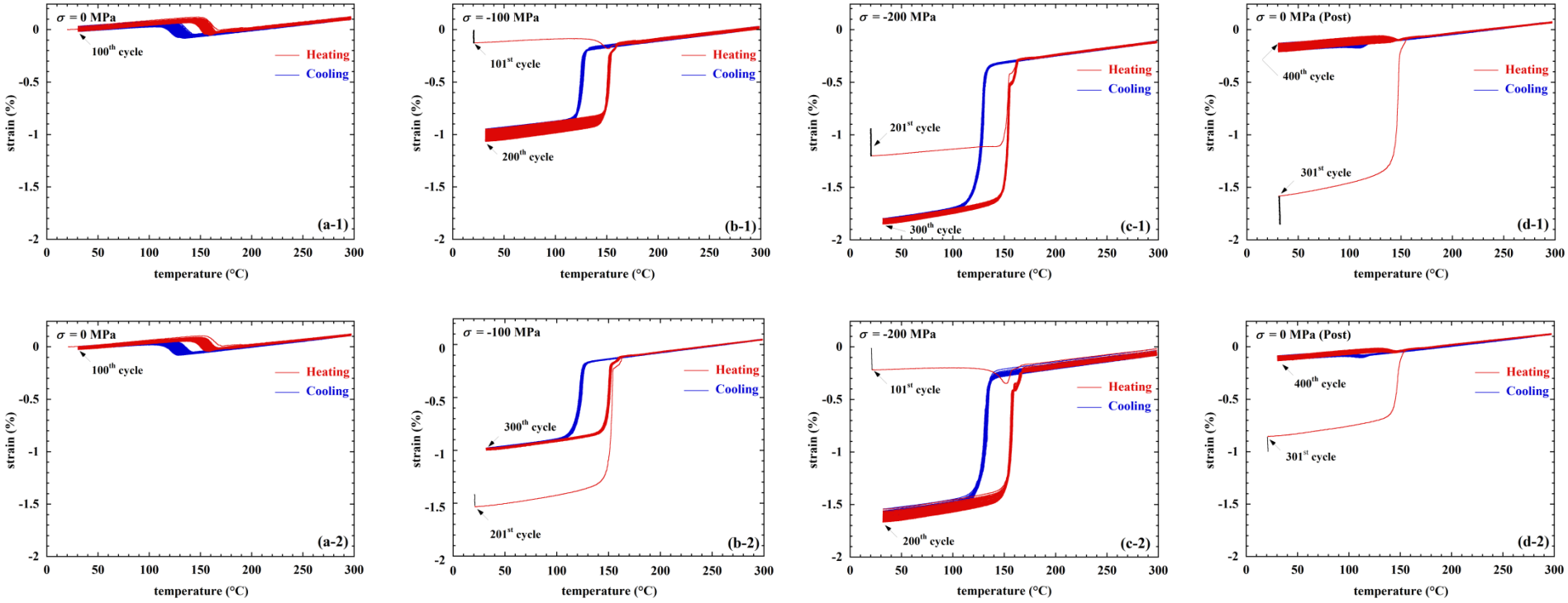
σ = 0 MPa
100th cycle
Heating
Cooling
(a-1)
σ = -100 MPa
101st cycle
200th cycle
(b-1)
σ = -200 MPa
201st cycle
300th cycle
(c-1)
σ = 0 MPa (Post)
400th cycle
301st cycle
(d-1)
(a-2)
(b-2)
(c-2)
(d-2)
strain (%)
temperature (°C)

Fig. 10

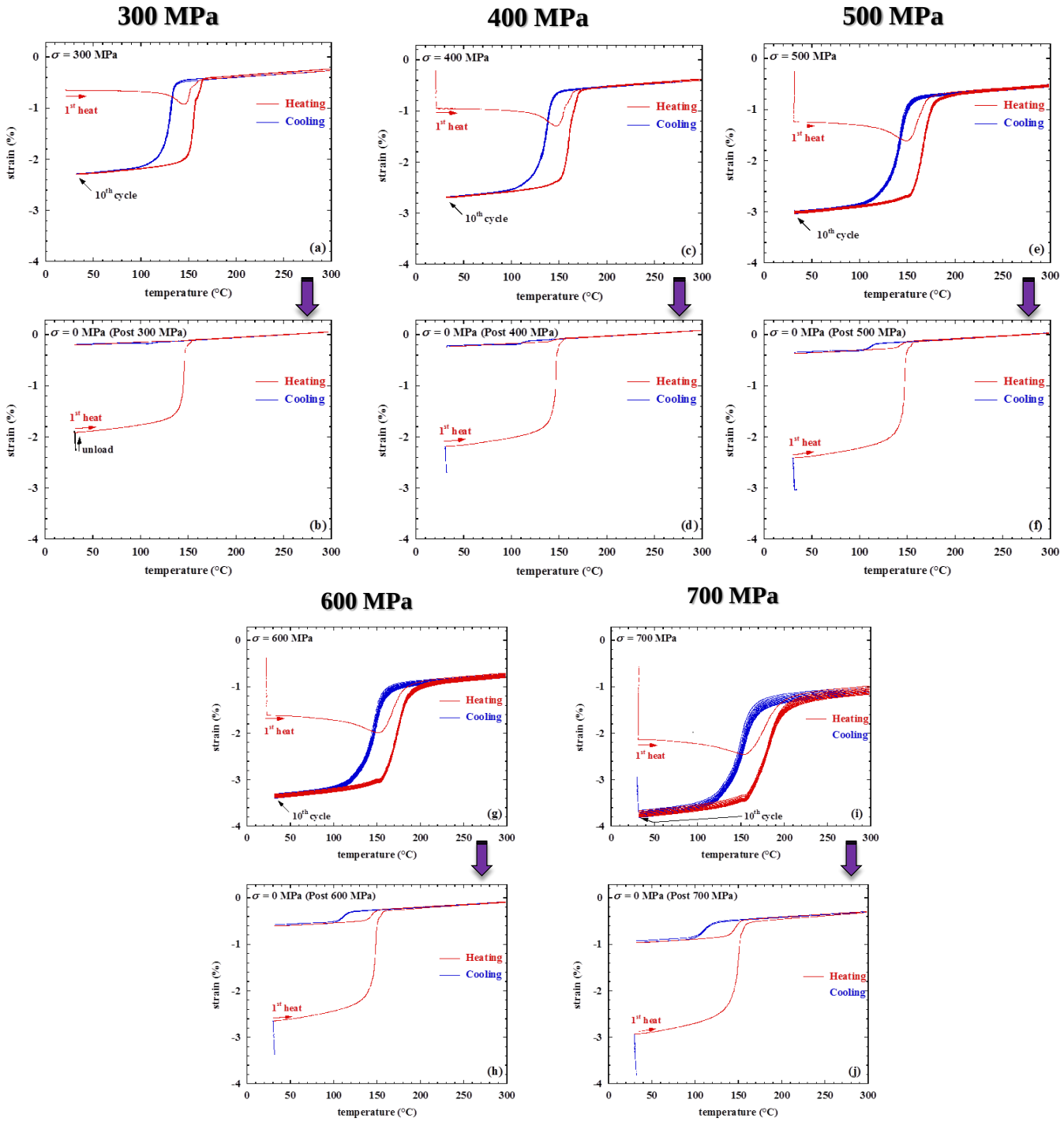
300 MPa
400 MPa
500 MPa
600 MPa
700 MPa
σ = 300 MPa
σ = 400 MPa
σ = 500 MPa
σ = 600 MPa
σ = 700 MPa
σ = 0 MPa (Post 300 MPa)
σ = 0 MPa (Post 400 MPa)
σ = 0 MPa (Post 500 MPa)
σ = 0 MPa (Post 600 MPa)
σ = 0 MPa (Post 700 MPa)
Heating
Cooling
1st heat
10th cycle
unload
strain (%)
temperature (°C)
(a)
(b)
(c)
(d)
(e)
(f)
(g)
(h)
(i)
(j)

Fig. 11

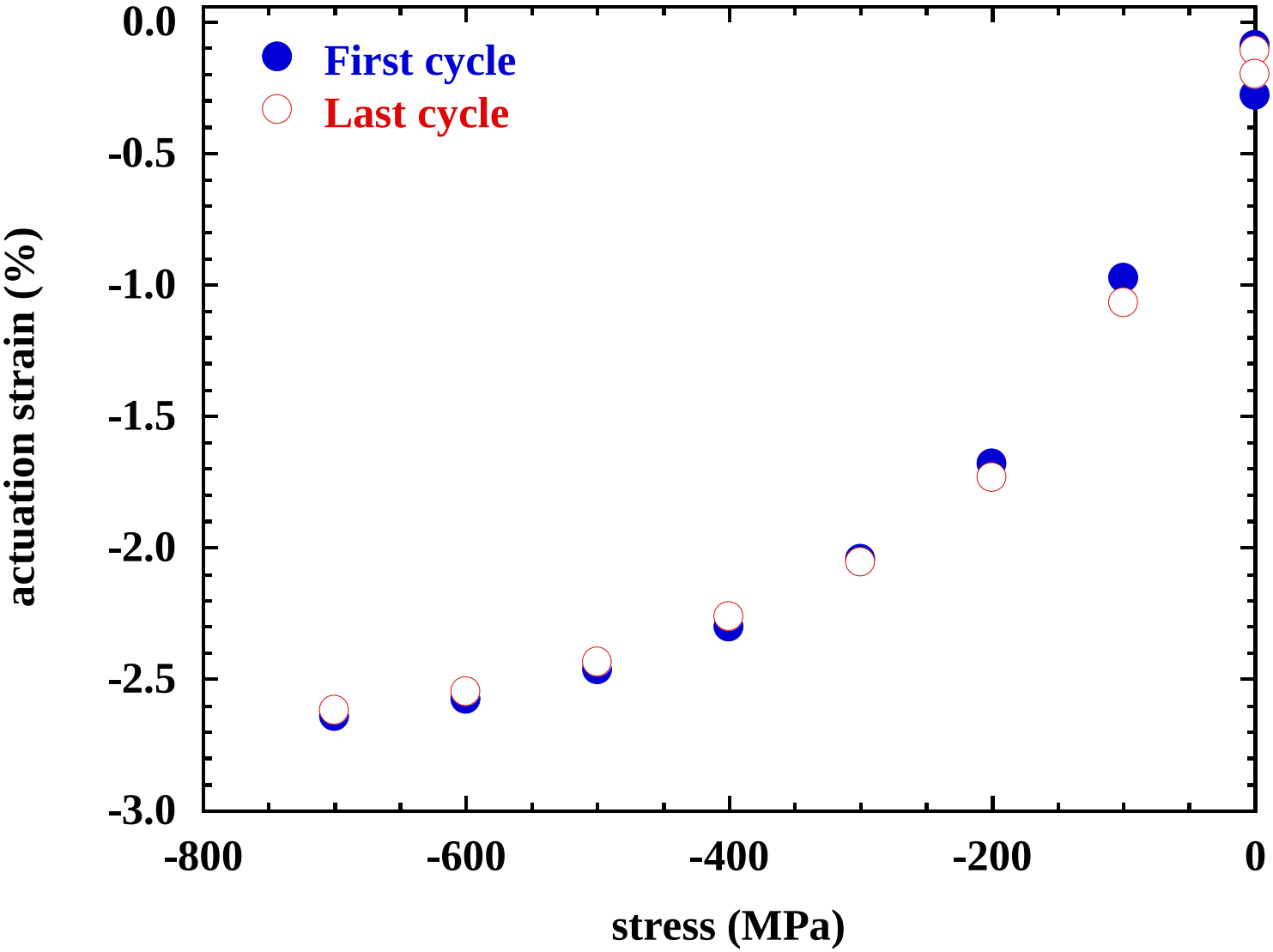
First cycle
Last cycle
actuation strain (%)
0.0
-0.5
-1.0
-1.5
-2.0
-2.5
-3.0
-800
-600
-400
-200
0
stress (MPa)

Fig. 12

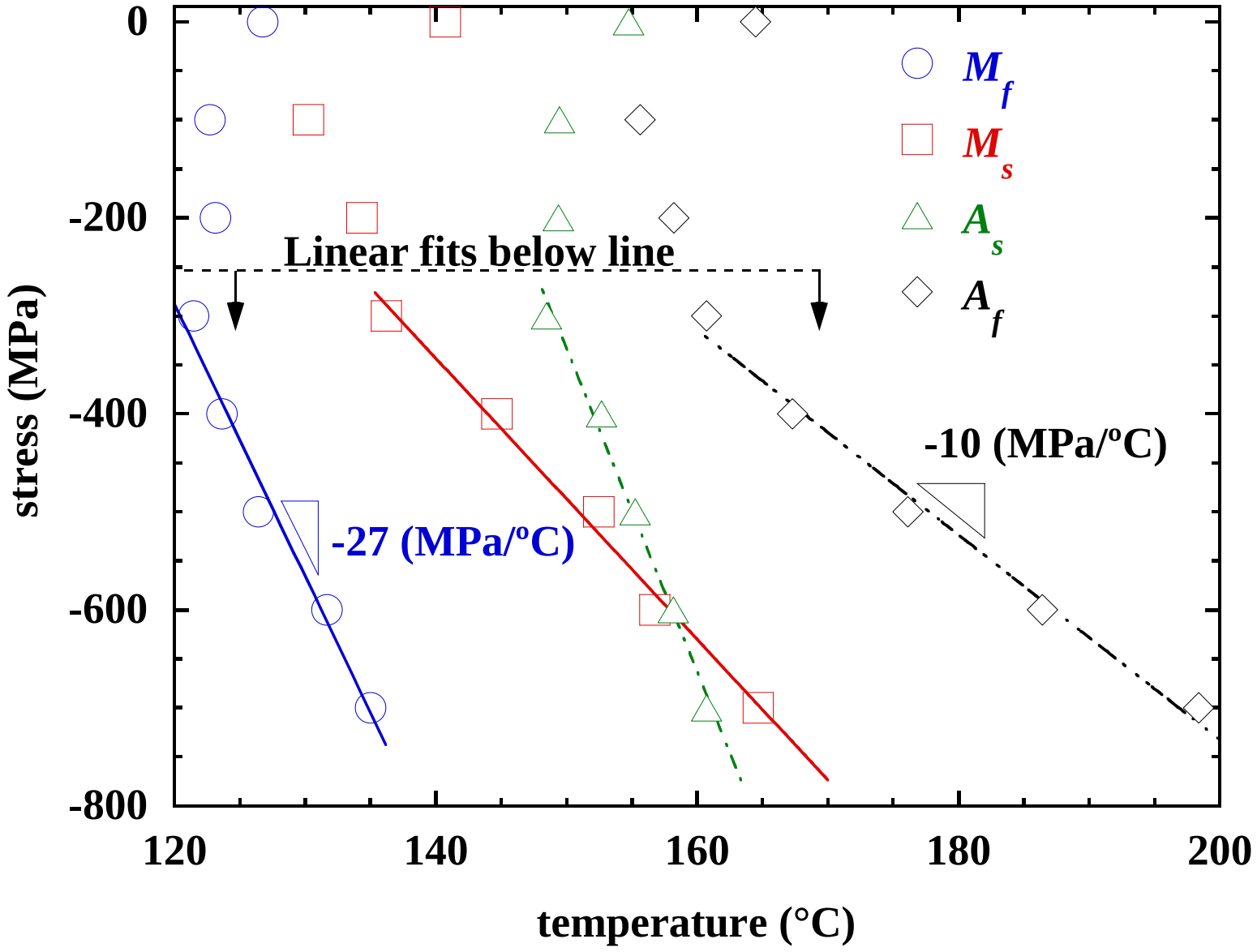
0
-200
-400
-600
-800
stress (MPa)
120
140
160
180
200
temperature (°C)
M_f
M_s
A_s
A_f
Linear fits below line
-27 (MPa/°C)
-10 (MPa/°C)

Fig. 13

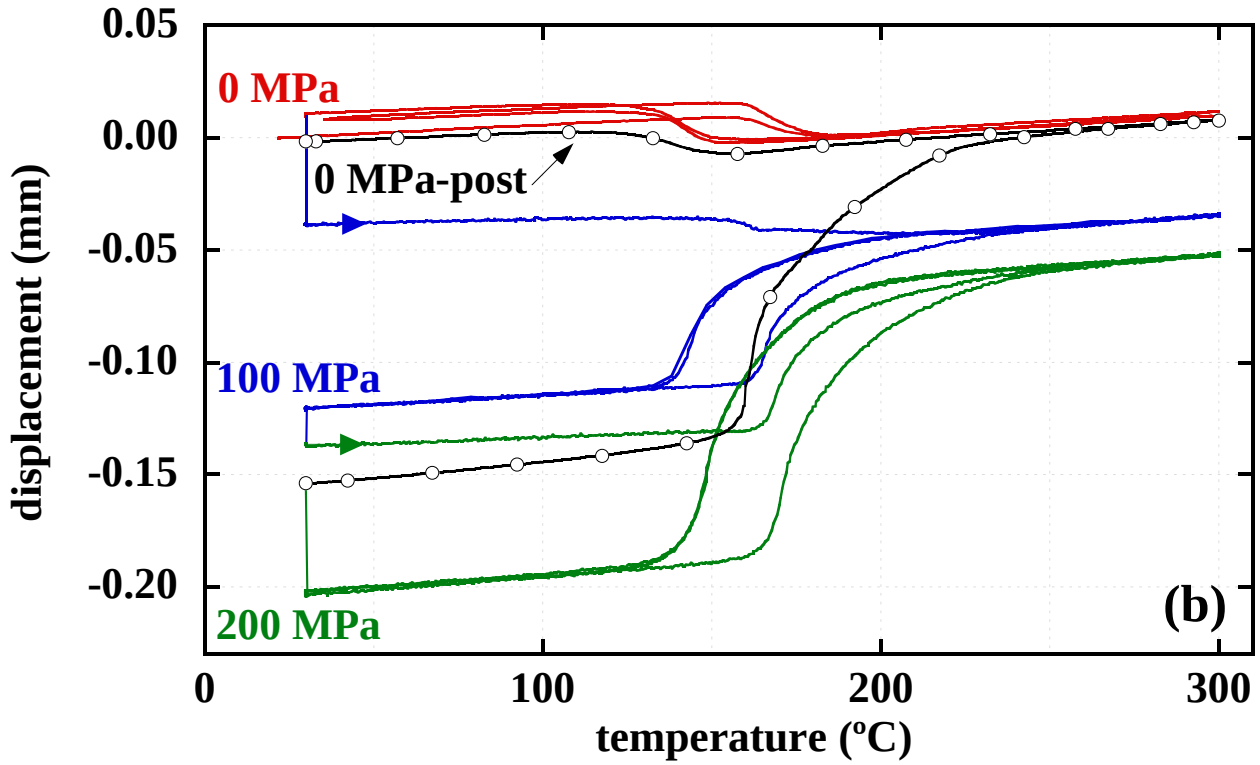
0.05
0.00
-0.05
-0.10
-0.15
-0.20
displacement (mm)
0 MPa
0 MPa-post
100 MPa
200 MPa
(b)
0
100
200
300
temperature (°C)

Fig. 14

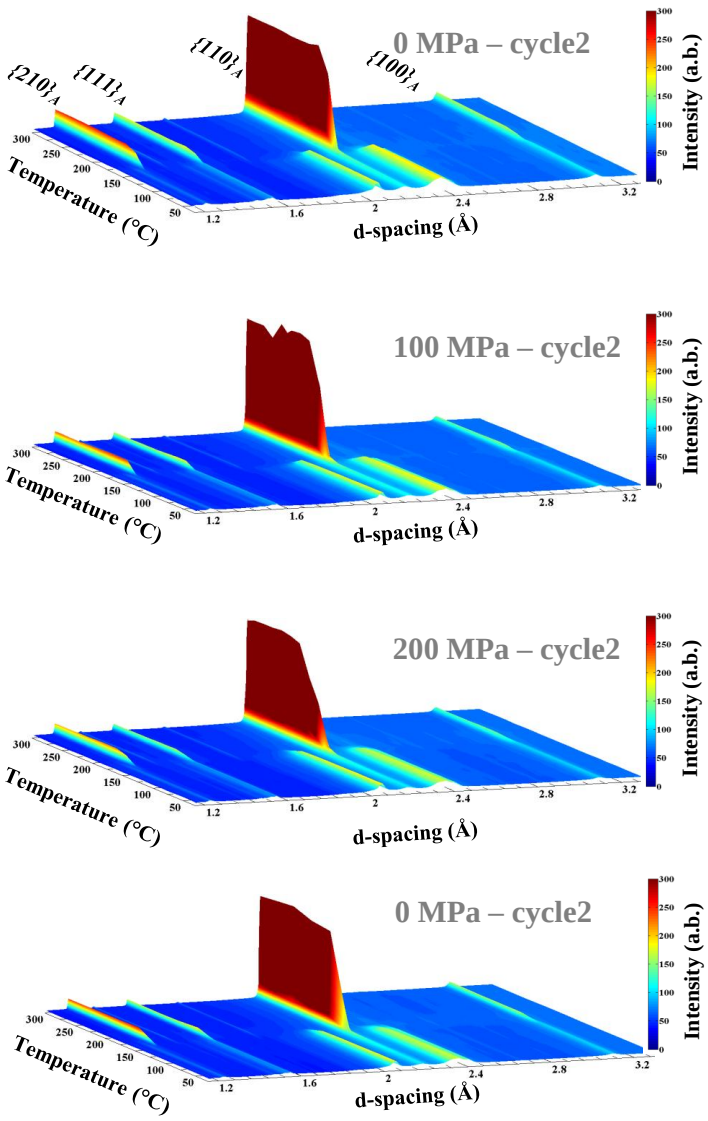
{210}A
{111}A
{110}A
{100}A
0 MPa – cycle2
Temperature (°C)
d-spacing (Å)
Intensity (a.b.)
100 MPa – cycle2
200 MPa – cycle2
0 MPa – cycle2

Fig. 15

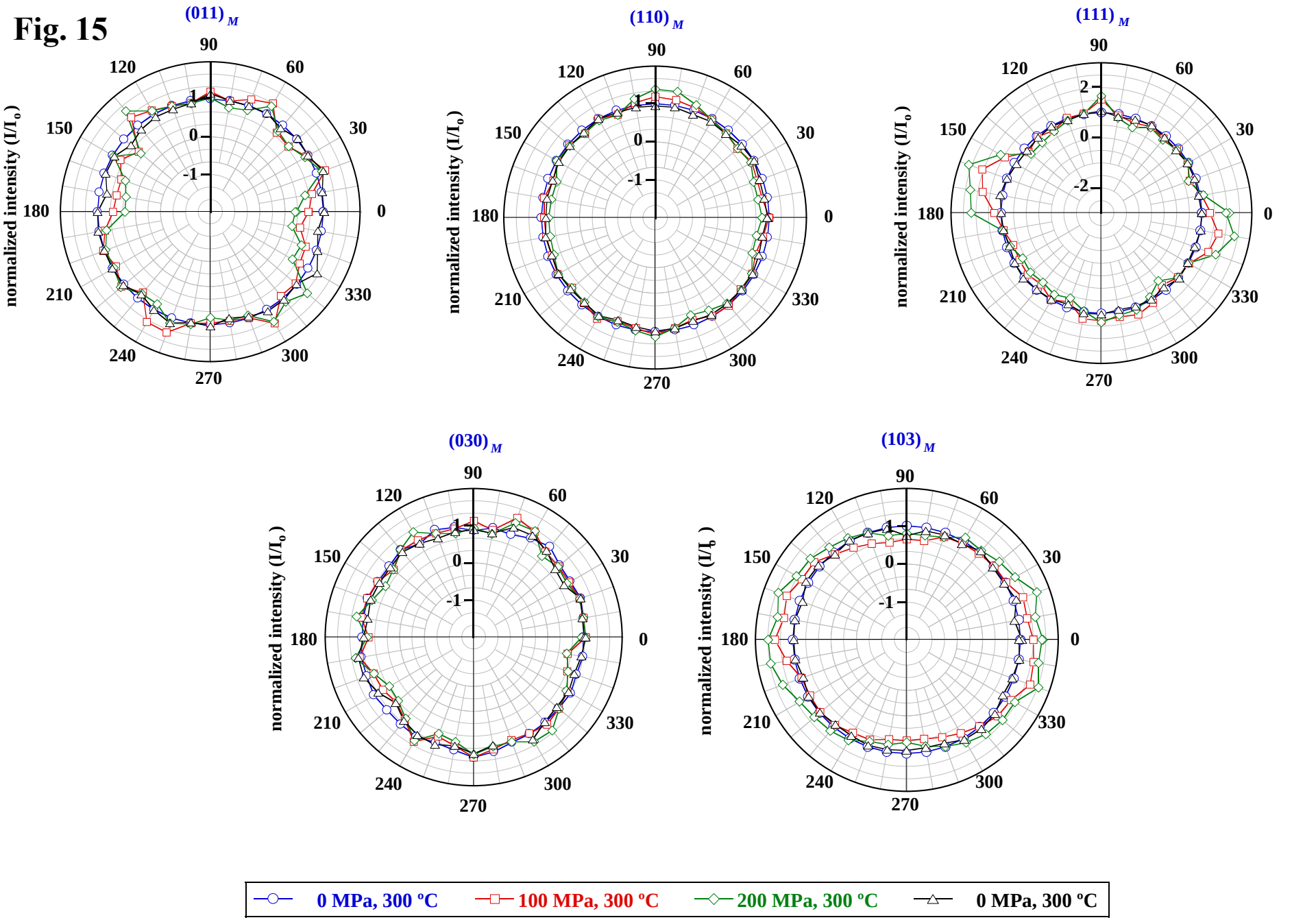
(011) M
(110) M
(111) M
(030) M
(103) M
normalized intensity (I/I0)
90
120
60
150
30
180
0
210
330
240
300
270
0 MPa, 300 °C
100 MPa, 300 °C
200 MPa, 300 °C
0 MPa, 300 °C

Fig. 16

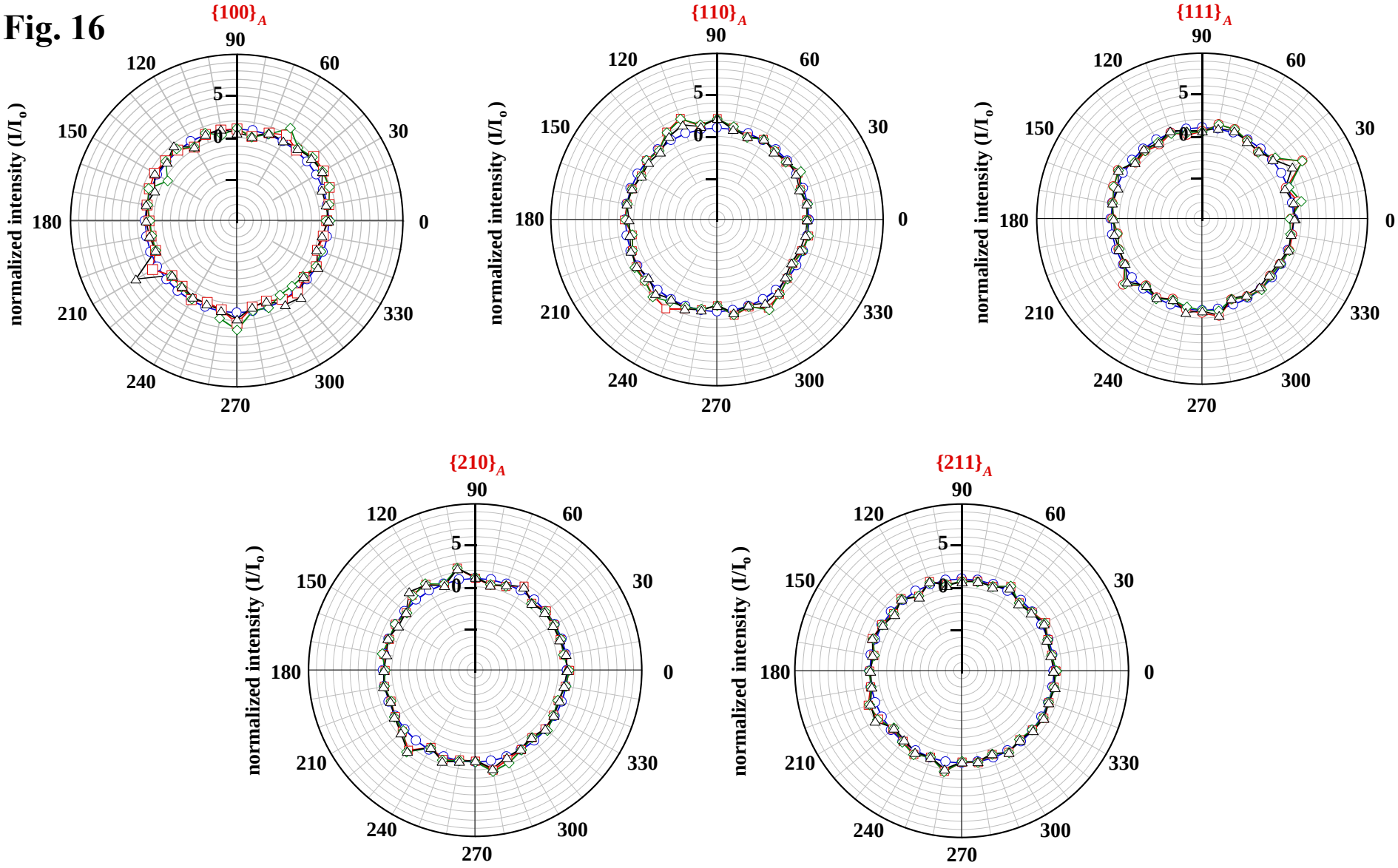
{100}A
{110}A
{111}A
{210}A
{211}A
normalized intensity (I/Io)
90
120
60
150
30
180
0
210
330
240
300
270
5
0
0 MPa, 300 °C
100 MPa, 300 °C
200 MPa, 300 °C
0 MPa, 300 °C

Fig. 17

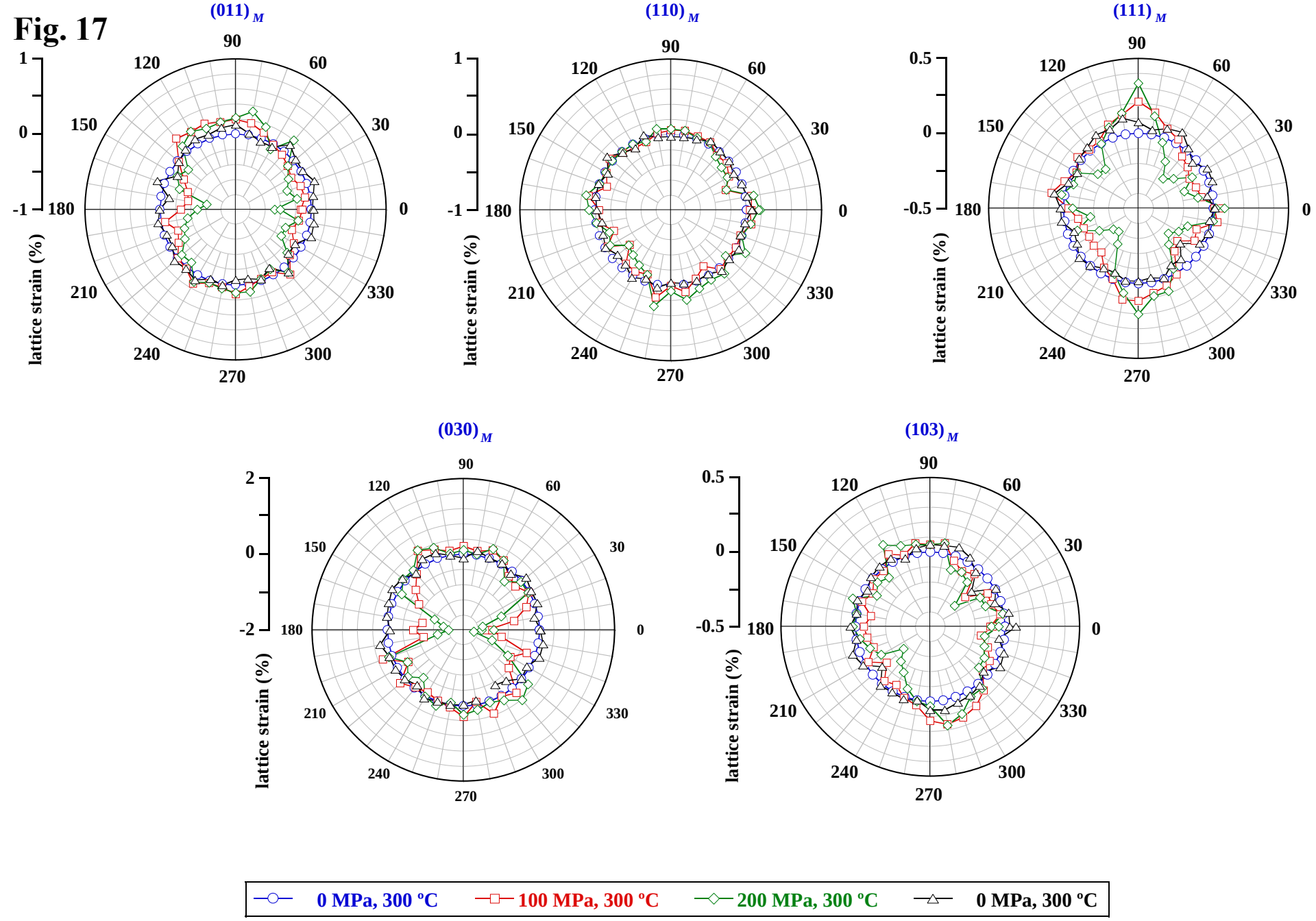
(011) M
(110) M
(111) M
(030) M
(103) M
lattice strain (%)
90
120
60
150
30
180
0
210
330
240
300
270
0 MPa, 300 °C
100 MPa, 300 °C
200 MPa, 300 °C
0 MPa, 300 °C

Fig. 18

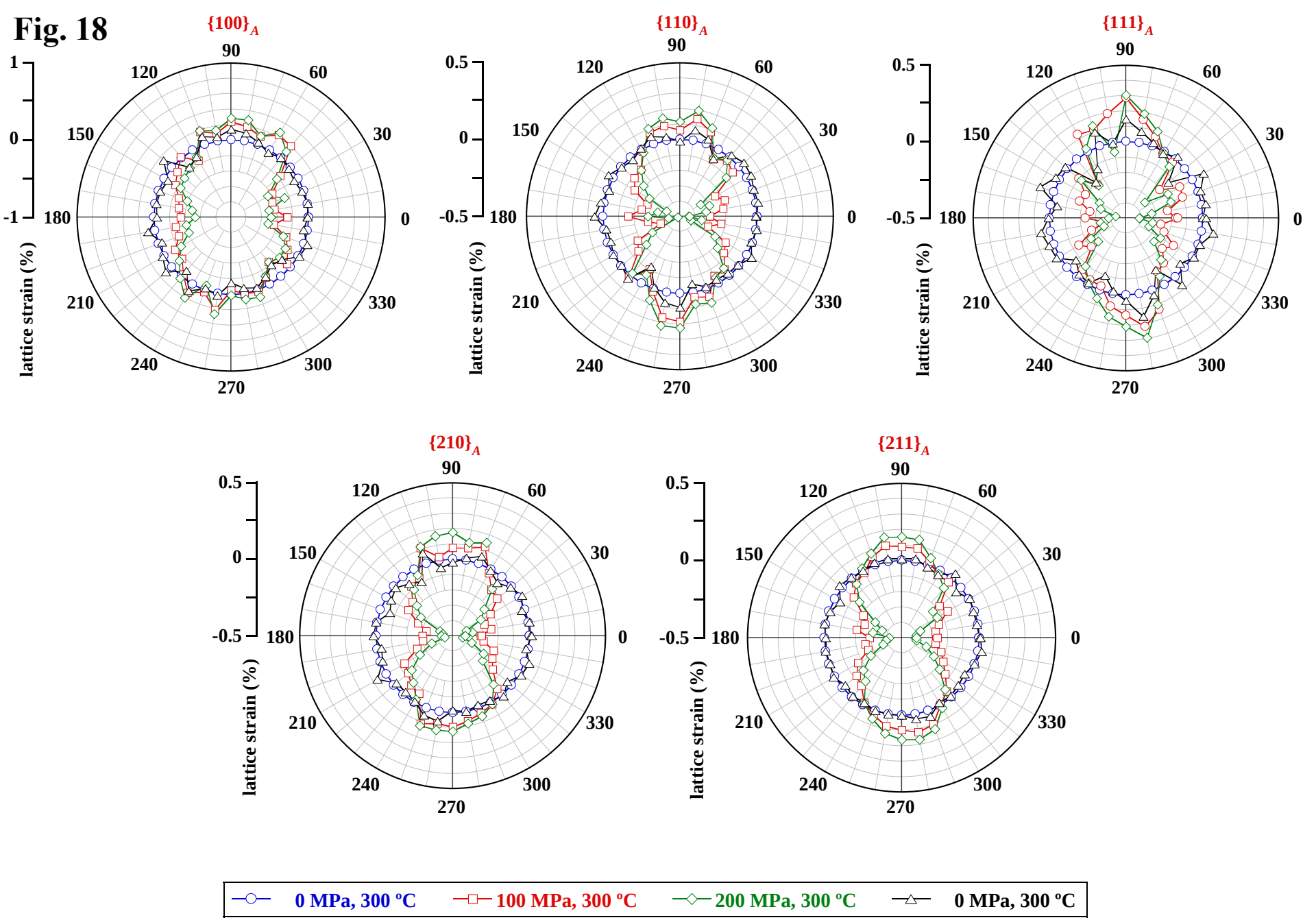
{100}A
{110}A
{111}A
{210}A
{211}A
lattice strain (%)
90
120
60
150
30
180
0
210
330
240
300
270
1
0
-1
0.5
-0.5
0 MPa, 300 °C
100 MPa, 300 °C
200 MPa, 300 °C
0 MPa, 300 °C

Not included